NANO LETTERS

December 2016
Volume 16, Number 12
pubs.acs.org/NanoLett

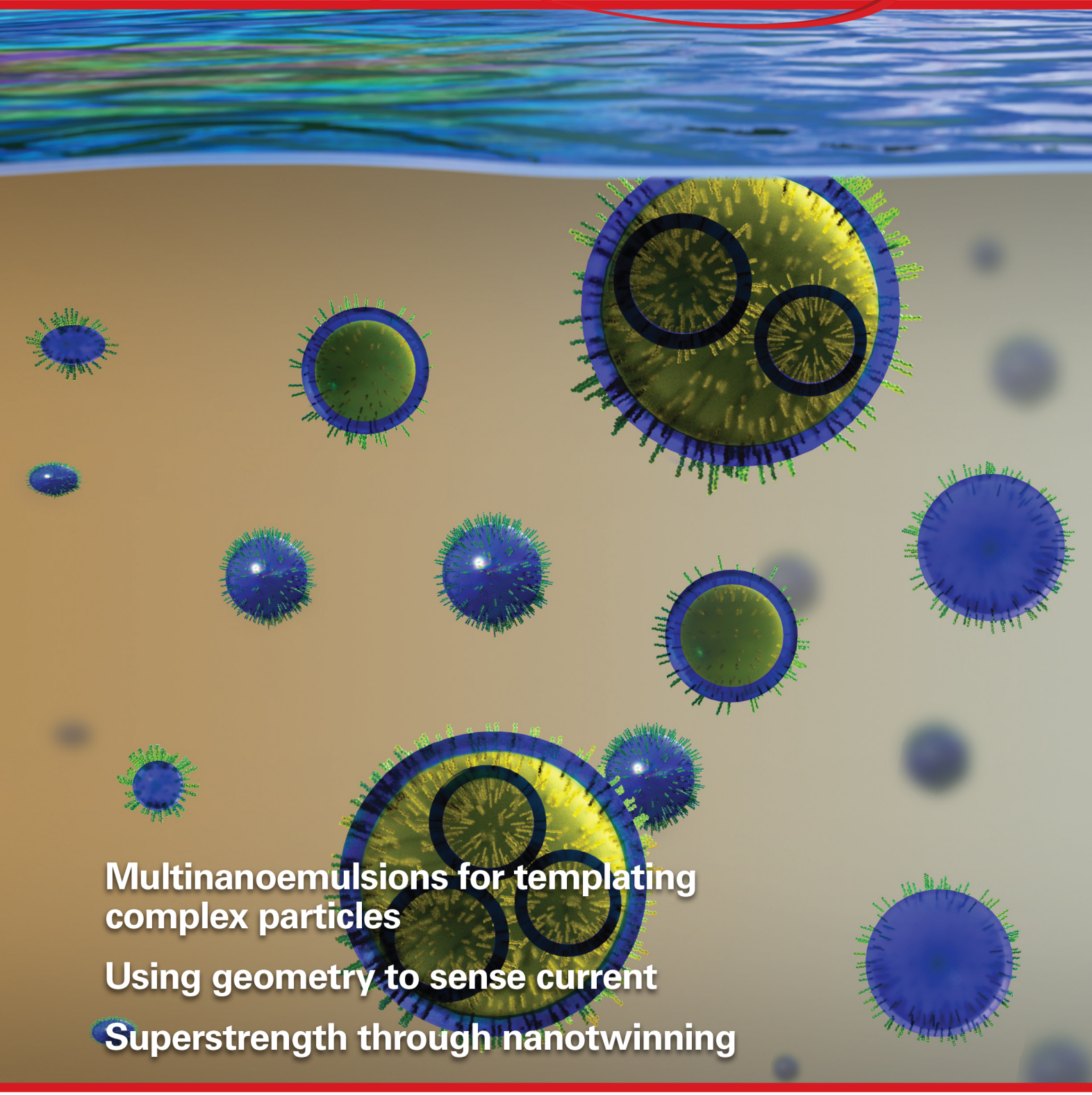

Multinanoemulsions for templating complex particles

Using geometry to sense current

Superstrength through nanotwinning

ACS Publications
Most Trusted. Most Cited. Most Read.

www.acs.org

NANO LETTERS

Letter

pubs.acs.org/NanoLett

Oil-in-Water-in-Oil Multinanoemulsions for Templating Complex Nanoparticles

Paula Malo de Molina, Mengwen Zhang, Alexandra V. Bayles, and Matthew E. Helgeson*

Department of Chemical Engineering, University of California Santa Barbara, 3357 Engineering II, Santa Barbara, California 93106, United States

Supporting Information

ABSTRACT: Complex nanoemulsions involving nanodroplets with a defined inner structure have great potential for encapsulation and templating applications. We report a method to form novel complex oil-in-water-in-oil nanoemulsions using a combination of high-energy processing with mixed nonionic surfactants that simultaneously achieve ultralow interfacial tension and frustrated curvature of the water−oil interface. The method produces multinanoemulsions possessing morphologies resembling water-swollen reverse vesicles with core−shell and multicore−shell morphologies of water in cyclohexane. A combination of macroscopic and microscopic characterization conclusively verifies and quantifies the complex morphologies, which vary systematically and reproducibly with water content for water volume fractions between 0.01 and 0.10. The complex morphologies are stable tens of hours, providing a route for their use as liquid templates for internally structured nanoparticles. As a demonstration, we test the complex nanoemulsions' ability to template complex polymer nanogels.

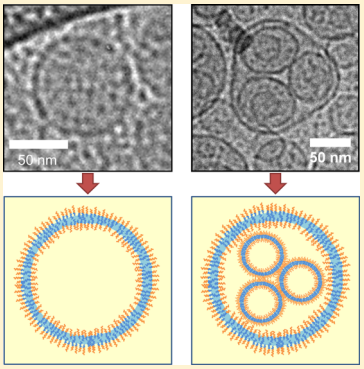

KEYWORDS: *Nanoemulsions, multiemulsions, nanoparticles, templating*

Emulsions are a critical technology for preparing and templating colloidal particles and structured materials including polymer latices and foams,[1] inorganic nanoparticles, and porous materials.[2,3] Recently, there have been significant advances in the development of processes to produce multiemulsions, that is, dispersed droplets of one liquid that contain smaller droplets of one or more other liquids.[4] Specifically, traditional sequential emulsification methods[5] have been surpassed by sophisticated microfluidic devices and accompanying emulsification strategies[6] to produce multiple emulsions with breathtaking control over their uniformity and internal morphology. The hierarchical structure of these multiemulsions have enabled a variety of applications for encapsulation and controlled drug release,[7,8] as well as templating of functional particles including hollow microcapsules,[9,10] vesicles,[11,12] colloidosomes,[13,14] and polymersomes.[15,16]

The aforementioned methods are limited in that they mostly produce droplets whose size (typically 10−100 μm)[17] lies just at the edge of the colloidal domain. By contrast, some of the most promising applications lie at the nanoscale, where multiemulsions could be used to create particles and materials with novel properties that take advantage of nanoscale phenomena. The synthesis of nanometer-scale double emulsions remains a significant challenge due to dramatic changes in energetic cost of formation and colloidal behavior when their size is driven to the nanoscale. As such, there have been only sparse reports of multinanoemulsions in the literature. Isolated examples include the formation of water-in-oil-in-water (W/O/W) double nanoemulsions using phase inversion temperature and pressure methods.[18,19] By contrast, oil-in-water-in-oil (O/W/O) double emulsions are, in general, less common and nanoemulsions of this type have not been reported to the best of our knowledge. This comes despite a clear need due to the abundance of aqueous-phase synthesis for polymer gels and sol−gel materials[20] for which O/W/O multiemulsions could provide a facile route to core−shell or multicompartment nanoparticles. Although there have been some reports of reverse vesicle structures containing water,[21,22] these structures only occur at small water contents (<1.5 vol %), which has prevented their use as templates for complex nanoparticles.

In this work, we demonstrate a method for the controlled formation of O/W/O double nanoemulsions containing relatively high water contents with a mixture of conventional nonionic cosurfactants using a one-step high-energy process. To do so, we exploit well-established strategies to use cosurfactants that dramatically lower the interfacial tension as well as bias the preferred interfacial curvature.[23] In this case, we also choose cosurfactants with highly asymmetric amphiphilic geometry (or surfactant packing parameter). We hypothesize that this asymmetry will lead to highly frustrated interfacial curvature under conditions of minimal interfacial tension and ultimately result in inversion of the curvature during the emulsification process. As such, high-energy emulsification provides a driving force for the formation of nanoscale structures, whereas the frustration of interfacial curvature leads to complex nanodroplet morphologies.

Received: May 21, 2016
Revised: July 20, 2016

DOI: 10.1021/acs.nanolett.6b02073
Nano Lett. XXXX, XXX, XXX−XXX

To achieve the necessary cosurfactant asymmetry and demonstrate the ability to form multinanoemulsions from conventional surfactants, we choose in this work the nonionic surfactants Span80 (S80) and Tween20 (T20). S80 has a rather large packing parameter that favors the formation of structures with negative curvature toward water, that is, W/O nanoemulsions,[24] whereas T20 has a bulkier hydrophilic headgroup and shorter hydrophobic tail and as a result will favor interfaces with positive curvature toward water, that is, O/W nanoemulsions.[25,26] The S80/T20 pair is known to produce ultralow surface tensions at hexane−water interfaces[27] and so is an ideal combination of surfactants in which to test the hypothesized method for creating multinanoemulsions.

Formation of Multinanoemulsions. To test the proposed method, we compare water-in-cyclohexane nanoemulsions prepared by ultrasonication with S80 alone to those prepared with a mixture of 5:3 S80/T20 (mol/mol) at the same total molar concentration (80 mM). First, we compare the turbidity, hydrodynamic radius, R_H, and viscosity, η, of the emulsified samples as a function of the water volume fraction, ϕ_w, (Figure 1). Solutions of S80 alone in cyclohexane are transparent (Figure 1a). For small ϕ_w, the fluid is turbid and R_H increases to 50 nm (Figure 1b). This indicates a transition from micelles to W/O nanoemulsions. For $0 < \phi_w < 0.02$, the droplet size remains relatively constant, and the turbidity increases as a consequence of the higher droplet volume fraction. Nanoemulsions with S80 alone are too turbid for accurate DLS measurements for $\phi_w > 0.02$ due to multiple scattering. The viscosity of the S80 nanoemulsions increases monotonically with ϕ_w (Figure 1c). To a first approximation, we consider the droplets as nondeformable spheres for which the relative viscosity, $\eta_r = \eta/\eta_0$, where η_0 is the oil viscosity, depends on the sphere volume fraction ϕ as[28]

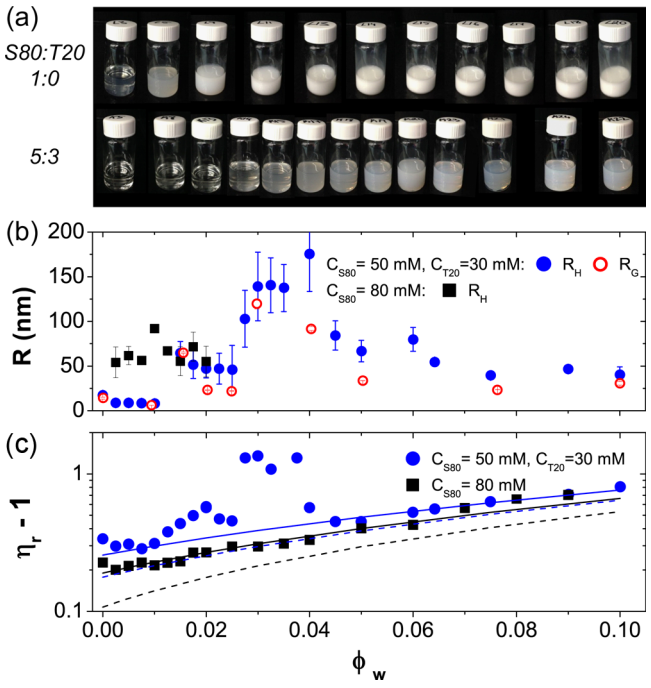

Figure 1. (a) Turbidity, (b) hydrodynamic radius R_H measured by DLS and radius of gyration R_G obtained from SANS, and (c) reduced viscosity for samples with S80/T20 80:0 and 50:30 mM as a function of the added water volume fraction. All measurements were done 20 min after sample preparation. The black (1:0) and blue (5:3) lines represent the hard sphere model with no solvation (dashed lines) and χ=0.5 of the surfactant chains (solid lines).

$$\eta_r - 1 = 2.5\phi + 10.05\phi^2 \quad (1)$$

For W/O emulsions, ϕ is the total volume fraction of the aqueous phase ($\phi = \phi_w + \phi_s$) where ϕ_s is the surfactant volume fraction. However, the surfactant chains are solvated with cyclohexane, and this extra solvent volume must be accounted for to describe the viscosity. Here, eq 1 perfectly describes the viscosity of the S80 nanoemulsions with a degree of solvation of the chains of χ = 0.5, that is, 50% of the volume containing surfactant chains is occupied by cyclohexane. Thus

$$\phi = \phi_w + \phi_{s,head} + \phi_{s,chains}\frac{1}{1-\chi} \quad (2)$$

where the subscripts on ϕ_s denote the surfactants' solvated ethoxylate head groups and hydrocarbon chains, respectively.

Employing the S80/T20 cosurfactant mixture dramatically changes the properties of the emulsions that are formed. In general, when comparing samples with identical ϕ_w between those containing S80/T20 and S80 alone, the former are much less turbid (Figure 1a). This suggests a different microstructure because the total volume fraction of the aqueous phase is only slightly larger than in the case of emulsions with S80 alone (due to the larger ethoxylated head of T20). For ϕ_w = 0, the system forms a transparent micellar solution with hydrodynamic radius R_H = 17 nm, that is, reverse micelles of surfactant. These reverse micelles are able to solubilize up to 0.01 of water with small variation in the size while maintaining transparency. This confirms the formation of reverse swollen micelles, that is, a thermodynamically stable W/O microemulsion phase. The size of the reverse microemulsion droplets is the same regardless of the fabrication method, that is, mechanical mixing or sonication, and they were stable for the duration of experiments. Microemulsions form in this case due to the ultralow interfacial tension of the mixed surfactant system that is able to overcome the dispersion entropy,[29] whereas with only S80 it is much larger.[30]

For $\phi_w > 0.015$, there is a dramatic increase of the droplet size without significant change in turbidity, indicating a change in the microstructure. In addition, η_r deviates from that predicted by eq 1 for uniform water spheres. Thus, the effective particle volume fraction is significantly larger than ϕ_w, suggesting the inclusion of cyclohexane in the droplets. R_H increases with further water addition, reaching a maximum at ϕ_w = 0.04 and then decreasing, ultimately limiting to 30 nm. For samples with $\phi_w > 0.05$, η_r recovers to that predicted for hard spheres. These measurements indicate that nanoemulsions with 5:3 S80/T20 at 80 mM surfactant have cyclohexane encapsulated in their interior for $0.015 < \phi_w < 0.05$, that is, they form multinanoemulsions.

Structural Characterization. To further investigate the nanostructures formed within the W/O nanoemulsions, we employed a combination of small angle neutron scattering (SANS) and cryo-transmission electron microscopy (cryo-TEM). For SANS (Figure 2a), contrast variation was employed using mixtures including perdeuterated water (D_2O) and cyclohexane (D_{12}-cyclohexane) to isolate the scattering from the water, surfactant, and oil films. For cryo-TEM, the hydrophilic contrast agent phosphotungstic acid (PTA) was added to increase the contrast between the water and cyclohexane phases. We have observed that PTA exhibits some affinity for the ethoxylated head groups of the surfactants, which

DOI: 10.1021/acs.nanolett.6b02073
Nano Lett. XXXX, XXX, XXX−XXX

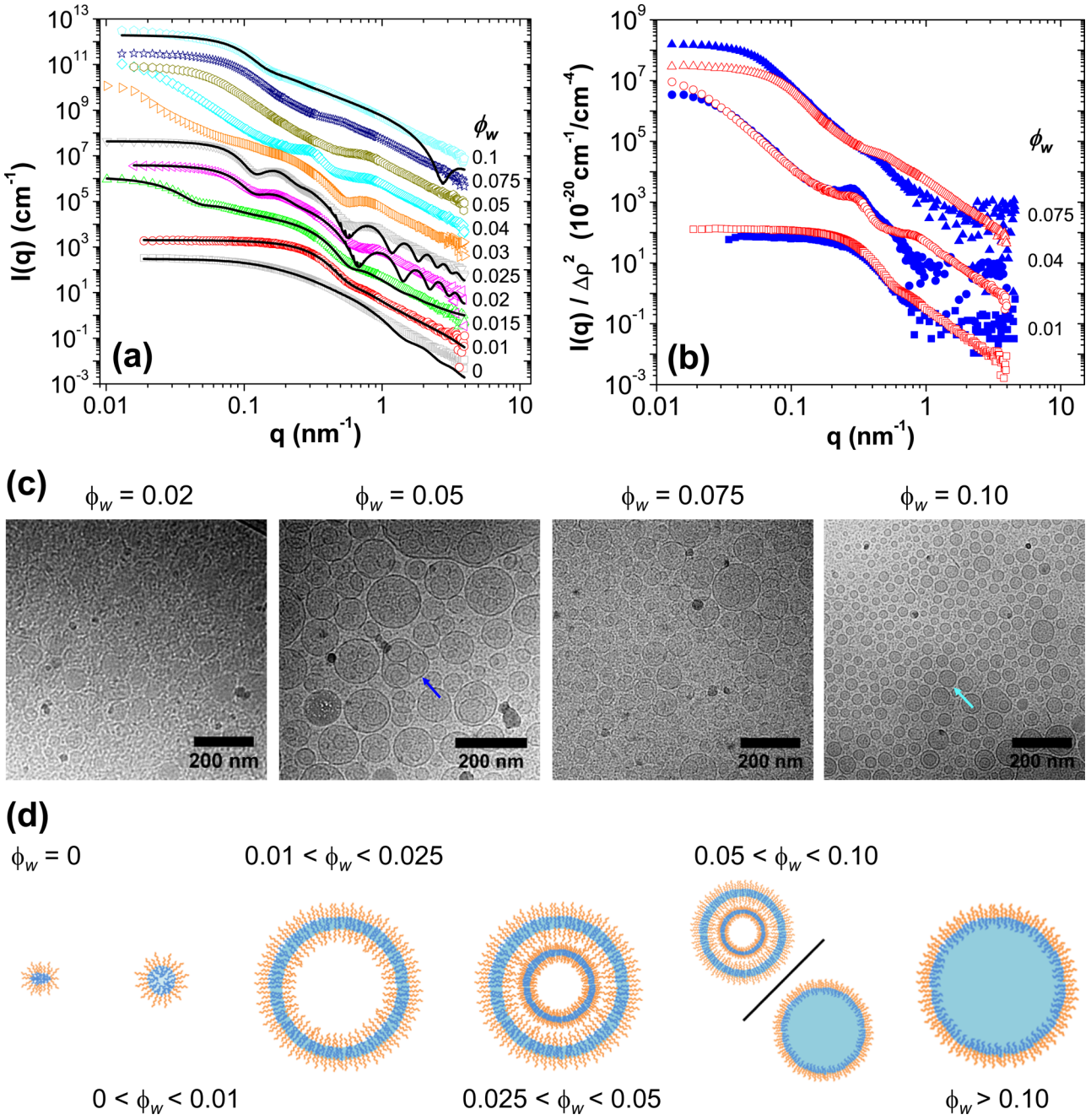

Figure 2. Microstructure of nanoemulsion samples with 50:30 mM S80/T20 and increasing water volume fraction ϕ_w. (a) SANS intensity curves of samples with H-surfactant/D_2O/D_{12}-cyclohexane (lines correspond to the model fit analysis described in the SI), (b) contrast variation SANS scattered intensity divided by the total contrast factor, $\Delta\rho^2$ measured in H-surfactant/D_2O/D_{12}-cyclohexane (red open points) and H-surfactant/8:2 H_2O/D_2O/H_{12}-cyclohexane (blue closed points), (c) representative cryo-TEM images, (red, dark blue, and light blue arrows represent swollen reverse vesicles, multicore structures, and uniform water droplets, respectively), and (d) schematic representation of the proposed structural evolution.

was confirmed through changes in the phase contrast upon the addition of the ethoxylated polymer poly(ethylene glycol) diacrylate (PEGDA) to the water phase (see SI Figure S4). This highlights the need for combined scattering and visualization methods in order to discern the morphologies of the multinanoemulsions.

Overall, the emulsions formed in the presence of S80/T20 exhibit a rich structural evolution with increasing ϕ_w (Figure 2). As a first analysis, we determined the radius of gyration, R_G, of the structures from the SANS spectra at low q-values (SI Table S1), which in all cases is in near agreement with values of R_H measured by DLS (Figure 1b, Table 1). Furthermore, the size of the nanostructures observed in cryo-TEM also agrees remarkably well with these measurements (Table 1), confirming that the samples prepared for both SANS and cryo-TEM exhibit the same nanostructures.

The shape and intensity of the SANS spectrum is dictated by the morphology and interactions of the microstructures. For $\phi_w = 0$, the scattering pattern shows a curve typical for small objects with a q^{-4} decay at high q. At lower q-values the intensity decays as $I \sim q^{-0.3}$, indicating that Span80/Tween20 mixed micelles are slightly elongated and fit to a triaxial ellipsoid model, confirming the asymmetric packing of surfactants. For $\phi_w = 0.01$, the curve has the typical features for core−shell structures with a shoulder

DOI: 10.1021/acs.nanolett.6b02073
Nano Lett. XXXX, XXX, XXX−XXX

Table 1. Nanodroplet Features Quantified by DLS, cryo-TEM, and SANS[a]

	DLS	cryo-TEM	SANS surfactant contrast			SANS interface contrast		
ϕ_w	R_H (nm)	R (nm)	R_G (nm)	R_{out} (nm)	t_{aq} (nm)	R_G (nm)	R_{out} (nm)	t_{aq} (nm)
0.000	17.4		13.9					
0.010	8.1		6.1	6.9	12.0	5.7	6.0	12.0
0.015	64.7		64.8					
0.020	47.2	27.9	23.1	28.6	6.5			
0.025	46.0	50.7	22.1	29.7	8.2			
0.030	139.1		119.5					
0.040	175.6		91.9			64.3		
0.050	66.7	56.3	33.7					
0.075	39.4	36.3	23.5			33.2		
0.10	40.5	24.2	30.7	22.8	41.0	32.7		

[a] R_H: Hydrodynamic radius from DLS; R: radius from cryo-TEM; R_G: radius of gyration from Guinier analysis; R_{out}, t_{aq}: outer radius and thickness of the aqueous phase, respectively, from SANS model analysis.

at $q \sim 0.6$ nm^{-1}. The high-q intensity decays with $I \sim q^{-4}$, reaches a plateau at low-q and fits well to a model for spherical water droplets surrounded by a surfactant shell (see SI). These observations and model fits confirm that for sufficiently low ϕ_w the water−cyclohexane−S80/T20 forms equilibrium spherical microemulsion structures with an aqueous core composed of D_2O and surfactant head groups of radius 6 nm and a surfactant chain shell of thickness 0.9 nm. These structures are too small to observe by cryo-TEM, because at this length scale they cannot be distinguished from the distortions of the continuous cyclohexane phase caused by beam damage.

Samples with ϕ_w = 0.02 and 0.025 exhibit features that are characteristic of thin water shells, that is, swollen reverse vesicle-type structures. Specifically, a shoulder at $q \sim 0.6$ nm^{-1} is observed in SANS, as well as a q^{-2} decay of the intensity at low q-values (Figure 2a). These features are characteristic of bilayer systems, where the shoulder indicates the correlated separation distance between adjacent surfactant layers. This is confirmed by contrast variation measurements. Figure 2b shows the scattering intensity normalized to the scattering contrast for two different contrasts, one in which both cyclohexane and water are perdeuterated (red open points), leaving only the contrast from the surfactants and containing perhydrogenated cyclohexane, and a ratio of H_2O/D_2O that matches the contrast of the surfactant headgroups (blue closed points), leaving only the contrast from the oil−water interface. For each water composition, the curves practically superimpose, confirming that the structure is the same for both contrasts. However, the curves for the surfactant contrast have an increase in scattering at high q-values, corresponding to the surfactant chains that are invisible in the interface contrast. Moreover, the shoulder at $q \sim 0.6$ nm^{-1} is retained only when the scattering contrast from the surfactant is present (Figure 2b), confirming that this feature arises from correlations between surfactant bilayers.

With the bilayer morphology established, the SANS data for ϕ_w = 0.02 and 0.025 fit well to a model consisting of a cyclohexane core and three shells (solvated chains−water phase-solvated chains). This is confirmed by cryo-TEM imaging (Figure 2c). Specifically, for ϕ_w = 0.02 we observe spherical structures with an average radius of ∼30 nm. The image contrast is the lowest in the continuous phase (cyclohexane), and is slightly darker for the spherical nanostructures. We also observe thin rings of darker contrast around the nanostructures, confirming the presence of thin water films. After understanding the structure of the samples with ϕ_w = 0.01 and 0.02, it is evident that the SANS intensity at 0.015 arises from a coexistence between spherical microemulsions and swollen reverse vesicles and is well modeled by a mixture of the two different structures (Figure 2a).

The samples with ϕ_w = 0.03, 0.04, and 0.05 exhibit a significantly different morphology. From the SANS data, we distinguish several features. At high q-values, the same shoulder and relative minimum at $q \sim 0.6$ nm^{-1} as in the vesicle-type structures appears, again suggesting a swollen bilayer structure with nearly identical water film thickness. However, at $q \sim 0.3$ nm^{-1} a new correlation peak appears, which grows and shifts to higher q-values as ϕ_w is increased, suggesting correlated structures that become more concentrated with increasing ϕ_w. These new, strong correlations do not coincide with a significant increase in viscosity of the fluid (Figure 1c) and DLS gives completely ergodic correlation functions for these samples (SI Figure S1). Therefore, these correlations must come from structuring inside the nanoemulsion droplets, rather than a suspension microstructure of the nanodroplets themselves. Although the SANS data from these structures defy fitting to a particular model, we discover the source of their internal structuring from cryo-TEM (Figure 2c). Specifically, for ϕ_w = 0.05 we observe multicore spherical structures with an overall radius of ∼50 nm and inner core radii of 20−30 nm. Both the inner and outer structures exhibit the same dark ring seen in the vesicle-type structures, suggesting that the structures formed are O/W/O/W/O nanodroplets, that is, swollen reverse multilamellar vesicles. As such, the correlation peak observed in SANS corresponds to structural correlations between the encapsulated core structures. The fact that this peak shifts to higher q-values with increasing ϕ_w suggests that in this range of morphologies an increase in water content results in an increase in the number density of cores. This is consistent with the observation that the water film thickness remains relatively constant over the entire range of ϕ_w, such that adding water results in more water films rather than an increase in the water film thickness.

For $\phi_w > 0.05$, a gradual transition from multicore structures to a different structure is observed. For ϕ_w = 0.075, the lower-q feature in SANS indicating correlations between cores begins to subside. At the same time, the average radius of the structures measured by SANS and cryo-TEM decreases significantly compared to samples with lower ϕ_w (Figure 2, Table 1). In the corresponding cryo-TEM images, we still observe multicore structures. However, some spherical structures without internal features also appear (Figure 2c). For ϕ_w = 0.10, we observe almost entirely circular nanostructures with relatively dark edges and no internal structures, although occasionally a multicore

DOI: 10.1021/acs.nanolett.6b02073
Nano Lett. XXXX, XXX, XXX−XXX

structure is observed. From cryo-TEM, it is difficult to discern whether these structures are uniform water-in-oil nanodroplets, or the reverse swollen vesicle-type structures observed at ϕ_w = 0.02.

To better discern the morphologies observed at relatively large ϕ_w, we performed cryo-TEM imaging on a sample with ϕ_w = 0.10, but containing only S80 and no T20 surfactant (SI Figure S5). This sample is known to produce uniform water droplets, so that their imaging features can be confidently evaluated. We see that upon the addition of the positive water stain PTA, the water droplets exhibit a thin shell of darker contrast. This suggests that cryo-TEM is unable to distinguish between swollen reverse vesicles and uniform water nanodroplets due to the low contrast between water and cyclohexane, even with the addition of PTA. Thus, in this particular case SANS provides more a more definitive determination of the structure for samples with ϕ_w = 0.10. Specifically, we find that the sample fits well to a core−shell model in which the scattering length density of the core is fixed to that of water and the scattering length density of the shell is fixed to that of the hydrated surfactant with only the size distribution left as an adjustable parameter. In other words, SANS indicates that the nanoemulsions obtained for this water content are uniform water nanodroplets, similar to the nanoemulsions produced when only S80 is used as the surfactant.

The overall sizes and dimensions of the nanodroplets obtained by all techniques are compared in Table 1. The best agreement is obtained for the microemulsion droplets where sample-to-sample variations are not expected. The hydrodynamic radius is larger than R_G measured by the SANS because it includes the solvation layer. The difference between the radius obtained in surfactant contrast and interface contrast corresponds to the thickness of the hydrophobic surfactant chains. Similar variations are expected to occur in the other samples. However, the nonequilibrium samples at higher water content exhibit some sample-to-sample size variation and their size is also time-dependent (Figure 3). Nevertheless, the agreement between the various comparable dimensions is relatively good and the trends with increasing ϕ_w are preserved across all techniques.

In total, Figure 2d summarizes the proposed evolution of morphologies observed in the water−cyclohexane−S80/T20 system with increasing ϕ_w. Upon addition of small amounts of water, we observe an equilibrium transition from elongated micelles to spherical microemulsion droplets. At higher water contents, nonequilibrium multinanoemulsions are observed, which exhibit morphologies including swollen reverse vesicles, multilamellar (multicore) vesicles, and finally spherical nanoemulsions in order of increasing ϕ_w. We note that to our knowledge this is one of the first reports of water-swollen reverse vesicles with nanoscale dimensions. Although reverse vesicles have been previously reported in systems containing mixtures of surfactants with different geometry[31] and ionic liquids,[32] here it is striking that reverse vesicles are only formed in the presence of a sufficient amount of water in the system.

Stability of Multinanoemulsions. The stability of these multinanoemulsion structures over time is an important factor for potential applications including nanoparticle templating (where short-time stability is critical) and product formulation (where long-term stability is also important). Figure 3 shows time series measurements of R_H for samples with varying water volume fraction, spanning the various morphologies identified in this work. As expected, the samples with $\phi_w \leq 0.01$ exhibiting equilibrium microemulsion (μE) morphologies are thermodynamically stable and have no observable change in size over the

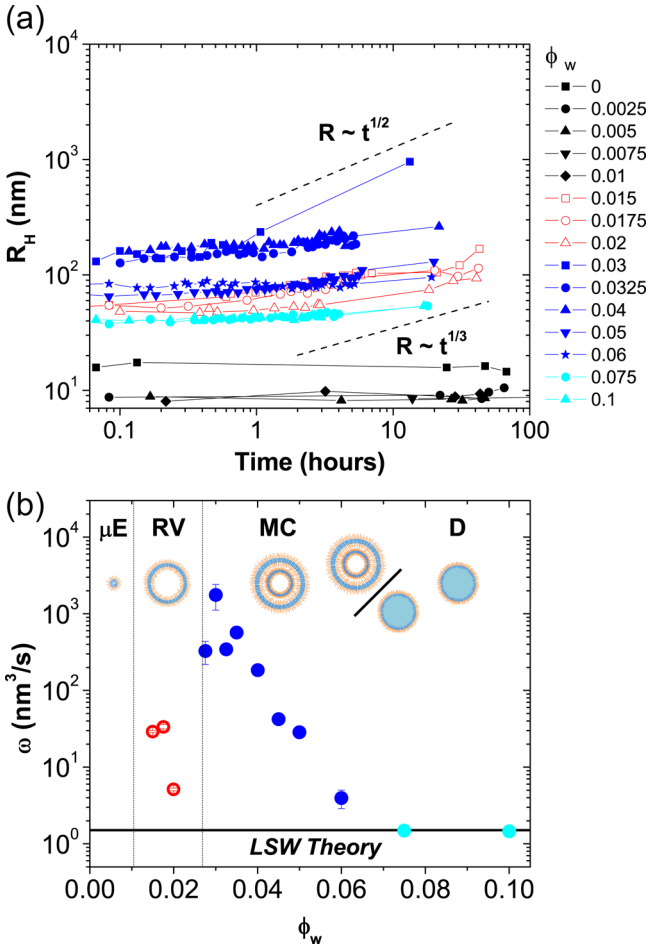

Figure 3. Stability of multinanoemulsions. (a) Time series of hydrodynamic radius obtained by DLS. Colors denote the various morphologies in (b). (b) Volumetric growth rates as a function of the water volume fraction. The line denotes the theoretical value for Ostwald ripening predicted by eq 3 of water droplets in cyclohexane.

course of measurement. Conversely, the nonequilibrium morphologies including swollen reverse vesicles (RV), multicore structures (MC), and uniform droplets (D) exhibit a relatively constant size at early times but thereafter begin increasing in size and eventually phase separate given sufficiently long time. It should be noted that the size evolution is different (less stable) if the solutions are not ultrasonicated. Comparisons of structures obtained by high- and low-energy emulsification are beyond the scope of this work. Nevertheless, we find that the multinanoemulsion structures are kinetically stable over a period of tens of hours, which exceeds the time scales for SANS measurement (thereby adding confidence in their interpretation) as well as that for many material chemistries (opening up the possibility of templating within them).

Here, we further analyze the microstructure in the time range leading up to phase separation. All of the complex nanoemulsions are relatively stable over a period of tens of hours with a size at longer times that increases as $R_H \sim t^{1/3}$. This scaling of the hydrodynamic radius indicates a constant volumetric growth rate, which is indicative of an Ostwald ripening process, that is, slow, molecular transfer of the dispersed phase between droplets predicted from entropic considerations.[33] The only exception to this trend is the sample with ϕ_w = 0.03, which corresponds to the maximal droplet size observed and exhibits a multicore

DOI: 10.1021/acs.nanolett.6b02073
Nano Lett. XXXX, XXX, XXX−XXX

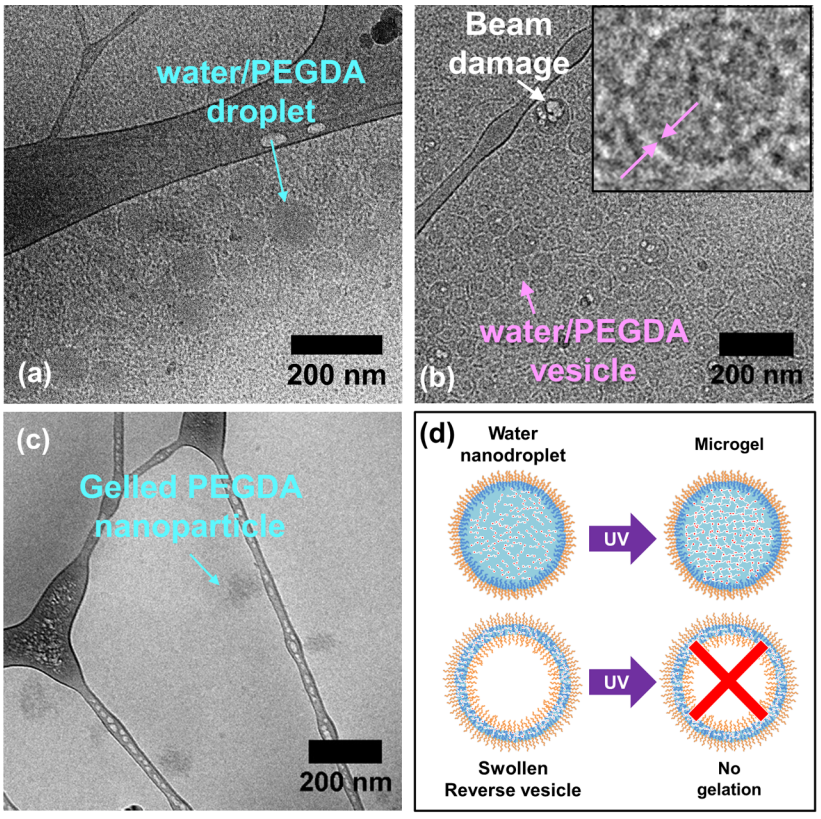

Figure 4. Templating of hydrogel nanoparticles using water/PEGDA−cyclohexane−S80/T20 nanoemulsions. Cryo-TEM images show structures before photo-cross-linking with (a) $\phi_{w+PEGDA}$ = 0.1 and (b) $\phi_{w+PEGDA}$ 0.02 (inset: enlarged view of a 70 nm swollen reverse vesicle). (c) Cryo-TEM image after photo-cross-linking and redispersion of nanoparticles in water from a nanoemulsion with $\phi_{w+PEGDA}$ = 0.1. (d) Polymerization scheme for nanoemulsion and swollen reverse vesicle templates.

morphology. This sample exhibits a growth in size that increases as $R_H \sim t^{1/2}$, that is, a constant surface area growth rate, which is typically associated with coalescence processes.[34]

To determine whether the droplet coarsening observed here is driven by internal ripening and coalescence would require a more detailed, time-resolved structural characterization by SANS and cryo-TEM to determine the inner structure with time. Such a study is beyond the scope of this work. Nevertheless, it is interesting to examine how the growth rate of the droplet size is influenced by the specific morphologies of the nanoemulsion droplets. For samples exhibiting growth driven by ripening, this is possible by comparing the linear volumetric growth rate of droplets. Specifically, we find that in all cases, R^3 has a linear relationship with time (see SI), allowing for the determination of the growth rates $\omega = dR^3/dt$ (Figure 3c). The growth rates increase with increasing water content of the nanoemulsion until ϕ_w = 0.03, where it reaches a maximum and then decreases.

In the idealized case, where droplets are spatially well-separated and uniformly distributed and growth occurs only through molecular transfer of water through a homogeneous cyclohexane phase due to its small (but nonzero) solubility, the rate of Ostwald ripening of the droplets can be predicted from the well-known Lifshitz−Slesov−Wagner (LSW) theory, which predicts

$$\omega = \frac{8C_{sat}^{W}\gamma_{OW}V_m^{W}D_0^{W}}{9\rho_W RT} \quad (3)$$

where C_{sat}^{W} is the molar saturation concentration of water in cyclohexane, γ_{OW} is the cyclohexane−water interfacial tension (this case in the presence of S80/T20 surfactant), V_m^{W} is the molar volume of water, D_0^{W} is the dilute self-diffusivity of water in cyclohexane, ρ_W is the density of water (in this case D_2O), R is the gas constant, and T the temperature. The growth rate predicted by eq 3 using LSW theory with $V_m{}^W$ as the molecular volume of water (18 mL/mol), $D_0{}^W$ as the diffusivity of water in cyclohexane predicted from the Wilke−Chang correlation (7.6×10^{-10} m^2/s)[35] and a water solubility in cyclohexane of 0.0333 g/L[36] is plotted in Figure 3b. Here, we have used a value of γ_{OW} = 0.01 mN/m for a mixture of Span 80 and Tween 20 at a hexadecane−water interface,[27] because we lack an accurate value for the water−cyclohexane−S80/T20 system.

The observed trends in droplet growth rate compared to LSW theory appear to depend significantly on the particular droplet morphology. The rate of growth of uniform water droplets is essentially equal to that predicted by LSW theory, validating the values we have used to compare to the experimental data. By contrast, both the vesicle-type (V) as well as the MC grow at a rate that is significantly faster than predicted by LSW theory. One possible explanation is that the water films both inside individual droplets and between droplets may undergo so-called "contact ripening", in which the rate of Ostwald ripening in the vicinity of the droplet may be significantly enhanced due to spontaneous fluctuations of the oil−water interface.[37] We also note that the MC structures exhibit the fastest rates of droplet growth, suggesting that internal coarsening processes may play a significant role in setting the growth rate of complex nanoemulsion droplets.

Overall, our studies suggest that the droplet morphology of nanoemulsions plays a significant role in setting the dominant

DOI: 10.1021/acs.nanolett.6b02073
Nano Lett. XXXX, XXX, XXX−XXX

mechanism(s) of droplet growth. We note, however, that the LSW theory does not take into account any complex internal morphology of the droplets, which might provide internal resistance to mass transfer of water, and thereby retard the rate of Ostwald ripening. As such, more detailed experiments and theories are needed to perform a more detailed study of the particular mechanisms of droplet instability in multinanoemulsions.

Toward Templating in W/O Multinanoemulsions. We have tested the use of these multinanoemulsions to template nanoparticles, specifically, polymer nanogels, for which bulk solution-phase syntheses typically allow poor control over particle size or internal morphology.[38] To do so, we first determined whether addition of a photocross-linkable polymeric hydrogel precursor, polyethylene diacrylate (PEGDA, M_n = 700), as well as a photoinitiator to the water phase prior to nanoemulsification retains the complex droplet morphologies observed in the water−cyclohexane−S80/T20 system. This was tested for both uniform water droplets (ϕ_w = 0.10) and swollen reverse vesicle-type droplets (ϕ_w = 0.02). Cryo-TEM experiments (Figure 4a,b) confirm that the droplets retain their previously observed morphologies upon addition of at least 10 vol % PEGDA to the aqueous phase of the nanoemulsion without significantly affecting their stability at short times (Figure S8, SI), potentially allowing for the formation of a cross-linked network of PEGDA in the water phase of the nanodroplets.[39]

We then tested the ability of PEGDA-laden nanoemulsions to template the morphology of PEGDA nanogel particles formed by UV-initiated free radical polymerization within the nanodroplets. If successful, one would thus expect the nanoemulsions with ϕ_w = 0.10 to form solid PEGDA hydrogel nanoparticles, and the nanoemulsion with ϕ_w = 0.02 to form core−shell nanocapsules composed of a thin PEGDA hydrogel shell with a cyclohexane core. To test this, samples were diluted after UV cross-linking with cyclohexane to water phase volume fractions corresponding to the microemulsion phase at ϕ_w < 0.01. In this way, if UV polymerization within the template droplets fail to produce an elastic PEGDA network, we would thus expect the particle size measured after dilution by DLS to revert to that of the equilibrium microemulsion phase.

We found that templating within uniform water nanodroplets (ϕ_w = 0.10) produces the anticipated result, that is, a suspension of nearly uniform PEGDA nanogel particles. Specifically, the hydrodynamic radius of the UV-cross-linked nanostructures is approximately 50 nm both before and after dilution (Table S7, SI), suggesting that cross-linking stabilizes the droplet morphology and size. The resulting nanoparticles were then separated from the cyclohexane phase and resuspended into deionized water. Cryo-TEM images of the resulting PGEDA nanogel suspensions (Figure 4c) indicate nearly spherical structures with a size that is nearly identical to that of the parent nanoemulsion, demonstrating the successful templating of uniform PEGDA hydrogel nanoparticles from W/O nanoemulsions with uniform droplets.

By contrast, UV-cross-linking within water-swollen reverse vesicle nanodroplets (ϕ_w = 0.02) fails to produce the anticipated PEGDA hydrogel nanocapsules. Specifically, the average hydrodynamic radius of the nanodroplets is approximately 50 nm both before and immediately after UV exposure but then decreases to 14 nm after subsequent dilution (Table S7, SI). Cryo-TEM images taken after separation of cyclohexane and purification into water are free from any objects that might indicate the formation of discrete structures from the vesicle-type nanoemulsions. Recalling that PEGDA and photoinitiator have no qualitative effect on the observed droplet morphology prior to UV exposure, this result indicates that the sequestration of PEGDA to a thin (4−6 nm) water film suppresses its ability to form a percolated polymer network. Several potential explanations for this include the possibility that (i) the reactivity of either the photoinitiator or polymerizing acrylic groups is suppressed at the oil−water interface (e.g., due to the presence of oxygen in the cyclohexane phase), which forms a nonreactive boundary layer comparable to the water film thickness;[40] (ii) interactions between PEGDA and the surfactants or the cyclohexane−water interface result in interfacial adsorption of acrylic groups,[41] inhibiting their polymerization upon UV exposure; (iii) the spatial confinement of PEGDA within the thin water shell prevents the formation of a mechanically robust polymeric network. Confirming which of these possible mechanisms is operative in the present experiments would require direct observation of the reactive species and/or PEGDA conformation within the water film during reaction and is left for future studies.

Summary. We have demonstrated formation of complex O/W/O multinanoemulsions using a mixture of two nonionic surfactants with opposite spontaneous curvature, S80 and T20. The presence of internal structuring of droplets is suggested by hydrodynamic radius and viscosity measurements, which both exhibit significant increases relative to that expected for uniform water droplets, and confirmed by a combination of contrast variation SANS and cryo-TEM. Our results may explain some observations made previously in W/O nanoemulsions with mixtures of nonionic surfactants, where it was found that the cosurfactant lowers the droplet size[42] and in some cases produces a viscosity enhancement similar to what is found here.[43]

SANS and cryo-TEM studies establish that a series of multinanoemulsions prepared at a constant cosurfactant composition exhibit a well-defined, rich, and reproducible set of morphologies that are determined by the dispersed water volume fraction. These morphologies include spherical microemulsions, unilamellar water-swollen reverse vesicles, multicore water-swollen multilamellar structures, and uniform spherical water nanodroplets. Further exploration of the role of cosurfactant composition should help to identify the particular physics that leads to well-defined multinanoemulsion structures and develop models to predict where such structures might appear in other material systems, both for O/W/O and W/O/W systems.

Finally, the reasonable kinetic stability of the reported O/W/O multinanoemulsions paves the way for their use in templating nanoparticles with complex morphology. The systems studied here already show great promise for creating uniform polymer hydrogel nanoparticles with well-controlled size, cross-link density, and elasticity. However, challenges remain with regards to templating within the vesicle-type structures due to apparent suppressed reactivity and/or formation of robust gel networks due to nanoscale confinement of reacting species to thin water films. Overcoming these challenges would provide a range of new template structures for multicompartment particles at the nanoscale and are thus the subject of ongoing studies.

■ ASSOCIATED CONTENT

Supporting Information

The Supporting Information is available free of charge on the ACS Publications website at DOI: 10.1021/acs.nanolett.6b02073.

DOI: 10.1021/acs.nanolett.6b02073
Nano Lett. XXXX, XXX, XXX−XXX

Experimental details; DLS autocorrelation functions; SANS analysis models and results; additional cryo-TEM images (PDF)

AUTHOR INFORMATION

Corresponding Author

*E-mail: helgeson@engineering.ucsb.edu.

Author Contributions

P.M.D.M., M.Z., and M.E.H. designed the experiments. P.M.D.M., M.Z., and A.V.B. carried out sample preparation. P.M.D.M. performed DLS and viscometry measurements, P.M.D.M. and A.V.B. performed SANS measurements, and M.Z. performed cryo-TEM experiments. P.M.D.M., M.Z., A.V.B. and M.E.H. prepared the manuscript.

Notes

The authors declare no competing financial interest.

ACKNOWLEDGMENTS

We thank Bruno F. B. Silva for help during preliminary SAXS test measurements, Frank Polzer for assistance with the Cryo-TEM, and Sahger Lad for assistance during the sample composition mapping. This work was funded in part by the Defense Threat Reduction Agency under the Natick Soldier Research, Development, and Engineering Center Agreement No. W911QY-13-2-0001. We acknowledge the support of the National Institute of Standards and Technology, U.S. Department of Commerce, in providing the neutron research facilities used in this work. The MRL Shared Experimental Facilities are supported by the MRSEC Program of the NSF under Award No. DMR 1121053, a member of the NSF-funded Materials Research Facilities Network (www.mrfn.org).

REFERENCES

(1) Menner, A.; Haibach, K.; Powell, R.; Bismarck, A. *Polymer* **2006**, *47* (22), 7628−7635.
(2) Pine, D. J.; Imhof, A. *Nature* **1997**, *389* (6654), 948−951.
(3) Zhang, H.; Cooper, A. I. *Soft Matter* **2005**, *1* (2), 107−113.
(4) Utada, A. S.; Lorenceau, E.; Link, D. R.; Kaplan, P. D.; Stone, H. A.; Weitz, D. A. *Science (Washington, DC, U. S.)* **2005**, *308* (5721), 537−541.
(5) Ficheux, M.; Bonakdar, L.; Bibette, J. *Langmuir* **1998**, *14* (11), 2702−2706.
(6) Arriaga, L. R.; Amstad, E.; Weitz, D. A. *Lab Chip* **2015**, *15* (16), 3335−3340.
(7) Muschiolik, G. *Curr. Opin. Colloid Interface Sci.* **2007**, *12* (4−5), 213−220.
(8) McClements, D. J. *Curr. Opin. Colloid Interface Sci.* **2012**, *17* (5), 235−245.
(9) Kim, S.-H.; Kim, J. W.; Cho, J.-C.; Weitz, D. a. *Lab Chip* **2011**, *11* (18), 3162−3166.
(10) Chen, P. W.; Erb, R. M.; Studart, A. R. *Langmuir* **2012**, *28* (1), 144−152.
(11) Arriaga, L. R.; Datta, S. S.; Kim, S.-H.; Amstad, E.; Kodger, T. E.; Monroy, F.; Weitz, D. a. *Small* **2014**, *10* (5), 950−956.
(12) Wang, T.; Deng, Y.; Geng, Y.; Gao, Z.; Zou, J.; Wang, Z. *Biochim. Biophys. Acta, Biomembr.* **2006**, *1758* (2), 222−231.
(13) Sander, J. S.; Studart, A. R. *Langmuir* **2011**, *27* (7), 3301−3307.
(14) Lee, D.; Weitz, D. A. *Adv. Mater.* **2008**, *20* (18), 3498−3503.
(15) Perro, A.; Nicolet, C.; Angly, J.; Lecommandoux, S.; Le Meins, J. F.; Colin, A. *Langmuir* **2011**, *27* (14), 9034−9042.
(16) Kamat, N. P.; Lee, M. H.; Lee, D.; Hammer, D. A. *Soft Matter* **2011**, *7* (21), 9863.
(17) Chu, L.-Y.; Utada, A. S.; Shah, R. K.; Kim, J.-W.; Weitz, D. A. *Angew. Chem.* **2007**, *119* (47), 9128−9132.
(18) Zhao, Y.; Zhang, J.; Wang, Q.; Li, J.; Han, B. *Phys. Chem. Chem. Phys.* **2011**, *13* (2), 684−689.
(19) Lee, H. S.; Morrison, E. D.; Frethem, C. D.; Zasadzinski, J. A.; McCormick, A. V. *Langmuir* **2014**, *30* (36), 10826−10833.
(20) Anton, N.; Benoit, J. P.; Saulnier, P. *J. Controlled Release* **2008**, *128* (3), 185−199.
(21) Nakamura, K.; Uemoto, A.; Imae, T.; Solans, C.; Kunieda, H. *J. Colloid Interface Sci.* **1995**, *170* (2), 367−373.
(22) Yang, D.; Zhao, J. *Colloid Polym. Sci.* **2016**, *294* (6), 1037−1043.
(23) Peng, L. C.; Liu, C. H.; Kwan, C. C.; Huang, K. F. *Colloids Surf., A* **2010**, *370* (1−3), 136−142.
(24) Capdevila, M.; Maestro, A.; Porras, M.; Gutiérrez, J. M. *J. Colloid Interface Sci.* **2010**, *345* (1), 27−33.
(25) Qian, C.; McClements, D. J. *Food Hydrocolloids* **2011**, *25* (5), 1000−1008.
(26) Erramreddy, V. V.; Ghosh, S. *Langmuir* **2014**, *30* (37), 11062−11074.
(27) Hashimoto, M.; Garstecki, P.; Stone, H. A.; Whitesides, G. M. *Soft Matter* **2008**, *4* (7), 1403.
(28) Thomas, D. G. *J. Colloid Sci.* **1965**, *20* (3), 267−277.
(29) Langevin, D. *Acc. Chem. Res.* **1988**, *21* (7), 255−260.
(30) Peltonen, L.; Yliruusi, J. *J. Colloid Interface Sci.* **2000**, *227* (1), 1−6.
(31) Tung, S. H.; Lee, H. Y.; Raghavan, S. R. *J. Am. Chem. Soc.* **2008**, *130* (27), 8813−8817.
(32) Rao, K. S.; So, S.; Kumar, A. *Chem. Commun. (Cambridge, U. K.)* **2013**, *49*, 8111−8113.
(33) Taylor, P. *Colloids Surf., A* **1995**, *99* (2−3), 175−185.
(34) Evans, F. D.; Wennerström, H. *The Colloidal Domain: Where Physics, Chemistry, Biology, and Technology Meet*; Advances in Interfacial Engineering; Wiley-VCH: Weinheim, 1996.
(35) Wilke, C. R.; Chang, P. *AIChE J.* **1955**, *1* (2), 264−270.
(36) Tsonopoulos, C.; Wilson, G. M. *AIChE J.* **1983**, *29* (6), 990−999.
(37) Roger, K.; Olsson, U.; Schweins, R.; Cabane, B. *Angew. Chem., Int. Ed.* **2015**, *54* (5), 1452−1455.
(38) Anselmo, A. C.; Zhang, M.; Kumar, S.; Vogus, D. R.; Menegatti, S.; Helgeson, M. E.; Mitragotri, S. *ACS Nano* **2015**, *9* (3), 3169−3177.
(39) Malo de Molina, P.; Lad, S.; Helgeson, M. E. *Macromolecules* **2015**, *48* (15), 5402−5411.
(40) Bong, K. W.; Bong, K. T.; Pregibon, D. C.; Doyle, P. S. *Angew. Chem., Int. Ed.* **2010**, *49* (1), 87−90.
(41) Kim, J.; Gao, Y.; Hebebrand, C.; Peirtsegaele, E.; Helgeson, M. E. *Soft Matter* **2013**, *9* (29), 6897.
(42) Porras, M.; Solans, C.; González, C.; Martínez, A.; Guinart, A.; Gutiérrez, J. M. *Colloids Surf., A* **2004**, *249* (1−3), 115−118.
(43) Chiesa, M.; Garg, J.; Kang, Y. T.; Chen, G. *Colloids Surf., A* **2008**, *326* (1−2), 67−72.

DOI: 10.1021/acs.nanolett.6b02073
Nano Lett. XXXX, XXX, XXX−XXX